Green Chemistry

PAPER

View Article Online
View Journal

Cite this: DOI: 10.1039/d5gc04693a

Light-driven and green Ullmann homocoupling with a Pd single-atom catalyst

Areti Moutsiou,[a] Theodore A. Gazis,[a] Luis A. Cipriano,[a] Mert Can Ince,[a] Ik Seon Kwon,[b] Nicolò Allasia,[a] Sadaf Fatima Jafri,[c,d] Elisa Borfecchia,[c,d] Lorenzo Mino,[c,d] Martin Sterrer,[e] Giovanni Di Liberto[f] and Gianvito Vilé *[a]

Received 7th September 2025,
Accepted 11th December 2025

DOI: 10.1039/d5gc04693a

rsc.li/greenchem

The sustainable synthesis of biaryl skeletons *via* Ullmann-type C–C coupling remains a challenge in organic synthesis. Herein, we report a series of Pd single-atom catalysts supported on mesoporous graphitic carbon nitride (CN_x) that promote the visible-light-driven homocoupling of aryl halides under ambient reaction conditions and with high efficiency and recyclability. Spectroscopic and microscopic analyses confirmed the atomic dispersion of Pd within CN_x and elucidated its local coordination environment, while demonstrating that the structural framework of the support remained intact upon metal incorporation. Mechanistic studies combining *operando* X-ray absorption spectroscopy and density functional theory revealed a reversible, light-induced change in Pd coordination, that is linked to the catalytic turnover. Finally, techno-economic analysis and life cycle assessment validated the sustainability of the protocol, highlighting its reduced environmental footprint compared to conventional approaches. Collectively, these findings demonstrate that photoactive single-atom catalysts are a promising platform for efficient, stable, and sustainable biaryl synthesis, paving the way for more sustainable and efficient C–C coupling methodologies.

Green foundation

1. We demonstrate that Ullmann homocoupling, a benchmark C–C bond-forming reaction, proceeds under green conditions using a palladium single-atom catalyst on carbon nitride ($Pd_1@CN_x$). This catalyst combines high activity and stability with minimal metal use, lowering costs and dependence on scarce palladium.
2. Our $Pd_1@CN_x$ cuts CO_2 emissions by ~70%, water use by ~75%, energy by 62%, and Pd precursor needs *vs.* nanoparticle systems by 93%. These results demonstrate how atomic-level catalyst design combined with light-driven activation can enable greener chemical transformations.
3. Greener advances could include solar-to-chemical integration, replacing LEDs with sunlight, bioderived supports and solvent-free or aqueous media, and circular strategies for Pd recovery and catalyst recycling. Such optimizations would move our approach toward a truly circular, carbon-neutral platform for sustainable C–C coupling.

Introduction

The Ullmann homocoupling reaction, long regarded as a cornerstone of synthetic chemistry, is indispensable for constructing biaryl scaffolds that constitute key motifs in pharmaceuticals, agrochemicals, and functional materials.[1] Initially performed with stoichiometric reagents, this transformation has progressively evolved into a catalytic protocol employing homogeneous transition metals, such as phosphine-ligated Pd(0)/Pd(II) complexes,[1,2] which enable lower coupling temperatures and offer broader substrate tolerance. Despite these advances, homogeneous systems remain prone to rapid deactivation, residual metal contamination in the final product, and challenges in purification and recycling.

Heterogeneous catalysts employing Pd nanoparticles[3] or bimetallic alloys[4,5] offer improved stability and reusability, but introduce new limitations, such as harsh operating conditions,[6] reliance on strong bases,[5,7] and the need for reductants.[4,6,7] Moreover, these catalysts suffer from low atom economy due to the low utilisation of bulk metal atoms.[8]

[a]*Department of Chemistry, Materials and Chemical Engineering "Giulio Natta", Politecnico di Milano, Piazza Leonardo da Vinci 32, 20133 Milano, Italy. E-mail: gianvito.vile@polimi.it*
[b]*Department of Energy Science and Engineering, Kunsan National University, 558 Daehak-ro, Gunsan-si, Republic of Korea*
[c]*Department of Chemistry, University of Torino, Via Pietro Giuria 7, Torino, 10125 Italy*
[d]*Nanostructured Interfaces and Surfaces (NIS) Interdepartmental Centre, University of Torino, Via Pietro Giuria 7, Torino, 10125 Italy*
[e]*Institute of Physics, University of Graz, Universitätsplatz 5, 8010 Graz, Austria*
[f]*Department of Materials Science, University of Milan Bicocca, Via Roberto Cozzi 55, 20125 Milano, Italy*

Furthermore, their catalytic activity is governed by unevenly distributed active sites, often located at edges or corners, and structural defects. This complicates active site identification and hinders efforts to correlate structure with performance. As a result, the rational design of heterogeneous Ullmann catalysts remains elusive.

Single-atom catalysts (SACs) have emerged as a transformative class of materials that bridge the gap between homogeneous and heterogeneous systems. By isolating individual metal atoms on solid supports, SACs combine the atomic efficiency and site uniformity of homogeneous catalysts with the robustness and reusability of heterogeneous systems.[8–11] In addition, their coordinatively unsaturated environment confers distinctive electronic properties to the metal atom that enhance reactant adsorption and catalytic activity.[12,13] However, their application to complex organic reactions has remained underexplored. For the Ullmann C–C homocoupling, only one example involving a bimetallic gold–palladium single-atom alloy catalyst[7] has been reported to date. While effective, the protocol required strong bases (NaOH) and additional reductants (ascorbic acid), which limit compatibility with sensitive substrates and add complexity to the operation.

Photocatalysis offers a sustainable route to overcome these challenges by enabling reactions under ambient conditions, exploiting light as a renewable energy source, and minimising the use of hazardous reagents.[14–17] Among the available catalysts,[18,19] carbon nitride (CN_x) stands out for its tuneable band structure, high thermal and chemical stability, and facile synthesis.[20] Moreover, its triazine cavities provide anchoring sites that can stabilise isolated metal atoms, making it an ideal support for SACs.[21–23] However, visible-light-driven Ullmann-type C–C coupling using SACs has not yet been demonstrated.

Herein, we report a family of Pd SACs supported on mesoporous graphitic carbon nitride ($Pd_1@CN_x$) that mediate the Ullmann homocoupling of aryl halides under ambient conditions and visible light irradiation. This system achieves efficient coupling under conditions significantly milder than those of conventional protocols. The results establish the untapped potential of photoactive SACs in C–C bond formation and highlight their broader promise for sustainable strategies in organic synthesis.

Results and discussion

Preparation and characterisation of the SACs

The introduction of Pd single atoms on mesoporous graphitic carbon nitride ($Pd_1@CN_x$) was achieved by co-condensation of K_2PdCl_4 with cyanamide, in the presence of SiO_2 nanoparticles as a hard template. This templating step assists in achieving a mesoporous structure while also stabilising the metal by lowering the surface energy of the metal atoms, which are otherwise prone to migration, particularly during pyrolysis.[24] A heating treatment at 550 °C, followed by template removal with (NH_4)HF_2, afforded the desired catalysts. The final composition and textural properties of the obtained catalysts are shown in Table 1.

Elemental CHN analysis revealed that all materials display a stoichiometric C/N ratio of *ca.* 0.60. The marginal variability in the ratios in both Pd-loaded and pristine CN_x samples can be ascribed to the incomplete polymerisation during the thermal process which gives rise to structural defects and residual impurities in the carbon nitride materials, in line with previous reports.[25] In addition, inductively coupled plasma-optical emission spectroscopy (ICP-OES) data demonstrated that varying the amount of metal precursor during synthesis allowed for controlled tuning of the Pd loading on the support, ranging from 0.43 to 1.32 wt%.

The crystallinity and phase purity of the Pd-based SACs was verified by X-ray diffraction (XRD) analysis (Fig. 1a). The XRD patterns displayed two distinctive diffraction peaks at 2θ angles of approximately 13° and 27°, corresponding to the trigonal nitrogen linkages of the triazine moieties and the interplanar stacking of aromatic rings, respectively.[26] Notably, no other diffraction peaks were present, implying the absence of metallic nanoparticles or other crystalline impurities in the samples. Moreover, across the Pd-loaded samples, the diffraction profiles remain essentially identical to pristine CN_x, indicating that the Pd loading does not significantly disturb the long-range order of the CN_x framework, even at the highest loading. To evaluate the surface area and porosity of the catalysts, N_2 physisorption studies at −196 °C were conducted. These textural measurements revealed high specific surface areas for all materials (Table 1). The high surface area and mesoporous nature of the catalysts allow for enhanced exposure of the active sites to the reaction mixture and improve light penetration, promoting more uniform photoexcitation of active sites.[27] Specifically, the obtained isotherms displayed type IV behaviour with H3 hysteresis loops (Fig. 1b) and average pore diameters of *ca.* 10 nm (Fig. 1c), confirming the mesoporous structure of the materials. Overall, the surface area and pore diameter of the Pd-loaded materials were greater than bare carbon nitride, revealing that the mesoporosity was preserved after Pd incorporation, and importantly, no pore collapse or decrease in surface area was observed.

Transmission electron microscopy (TEM) analysis shows a lack of discernible metal clusters, indicating well-dispersed Pd

Table 1 Elemental composition and textural properties of catalytic materials

Catalyst	C[a] (wt%)	N[a] (wt%)	H[a] (wt%)	Pd[b] (wt%)	S_{BET}[c] ($m^2\ g^{-1}$)
CN_x	30.4	52.6	1.80	—	185
0.43-$Pd_1@CN_x$	31.4	53.1	1.97	0.43	279
0.67-$Pd_1@CN_x$	30.9	52.2	2.42	0.67	254
1.32-$Pd_1@CN_x$	32.4	54.7	2.10	1.32	246

[a] CHN elemental analysis. [b] ICP-OES data. [c] BET method applied on the adsorption branch of the N_2 isotherm in the $0.05 < p/p_0 < 0.3$ range.

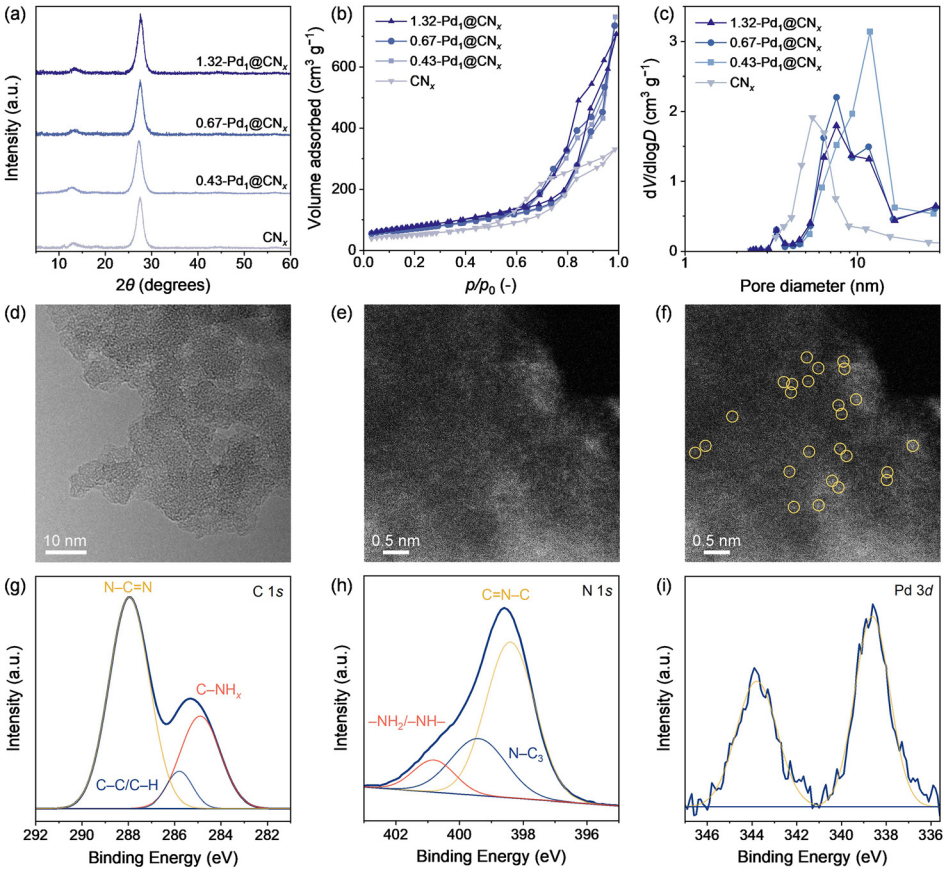

Fig. 1 (a) XRD patterns, (b) N_2 physisorption isotherms, and (c) pore size distribution calculated using the BJH method from the desorption branch of CN_x and $Pd_1@CN_x$ catalysts. (d) TEM image and (e) HR-TEM image of 1.32-$Pd_1@CN_x$ with (f) selected single atoms marked with yellow circles. (g) C 1s, (h) N 1s, and (i) Pd 3d XPS of 1.32-$Pd_1@CN_x$.

species within the CN_x framework (Fig. 1d). Notably, using high-resolution TEM (HR-TEM), we could observe individual metal atoms uniformly dispersed on the support (Fig. 1e). The micrograph revealed isolated bright spots corresponding to single Pd atoms, confirming their dispersion at the atomic level and proving that agglomeration of Pd atoms into larger clusters and nanoparticles did not occur during catalyst synthesis. To evaluate the role of SiO_2 in Pd dispersion, a reference material was prepared under identical conditions but without the addition of SiO_2. TEM analysis of the synthesised material revealed the presence of Pd aggregates (Fig. S1), demonstrating that single-atom dispersion is achieved better when a highly-porous material is used as support.

Further insights into the chemical state of carbon nitride and active Pd species on its surface were obtained by X-ray photoelectron spectroscopy (XPS). The analysis was performed on the highest-loading 1.32-$Pd_1@CN_x$, as a representative catalyst, since the stronger Pd signal enhanced sensitivity and ensured reliable analysis of the active sites. Two peaks were observed in the Pd 3d spectrum (Fig. 1i), corresponding to Pd $3d_{5/2}$ and Pd $3d_{3/2}$ signals, with a Pd $3d_{5/2}$ binding energy of 338.7 eV, assigned to positively charged Pd species.[28,29] The C 1s signal (Fig. 1g) consists of three contributions, with binding energies of 287.9 eV, 285.7 eV, and 284.7 eV that are ascribed to sp^2-hybridised N–C=N bonds in the tri-*s*-triazine ring of carbon nitride, $C–NH_x$ bonds, and adventitious carbon (C–C/C–H). The signal present in the N 1s spectrum (Fig. 1h) could be deconvoluted into three peaks at 400.8 eV, 399.4 eV, and 398.4 eV, corresponding to pyrrolic nitrogen ($C–NH_2$ and C–NH–C), graphitic nitrogen ($N–C_3$), and pyridinic nitrogen (C=N–C).[30]

To comprehend the electronic and local structure of $Pd_1@CN_x$, X-ray absorption spectroscopy (XAS) was utilised. Analysis was performed on 1.32-$Pd_1@CN_x$ to understand the electronic and local structure from its Pd and N *K* edges, using PdO powder and Pd foil as references in the Pd *K* edge XAS data. Fig. 2a illustrates the X-ray absorption near edge structure (XANES) for the Pd *K* edge, where 1.32-$Pd_1@CN_x$ displays a distinct spectral shape compared to Pd and PdO reference samples, indicating a different local atomic environment. This confirms that the local structure of 1.32-$Pd_1@CN_x$ is neither metallic Pd nor PdO.

Fig. 2b displays the extended X-ray absorption fine structure (EXAFS) data for the Pd *K* edge through the Fourier transformation of the X-ray absorption spectrum from rising edges to 1200 eV. Specifically, 1.32-$Pd_1@CN_x$ displays non-phase-cor-

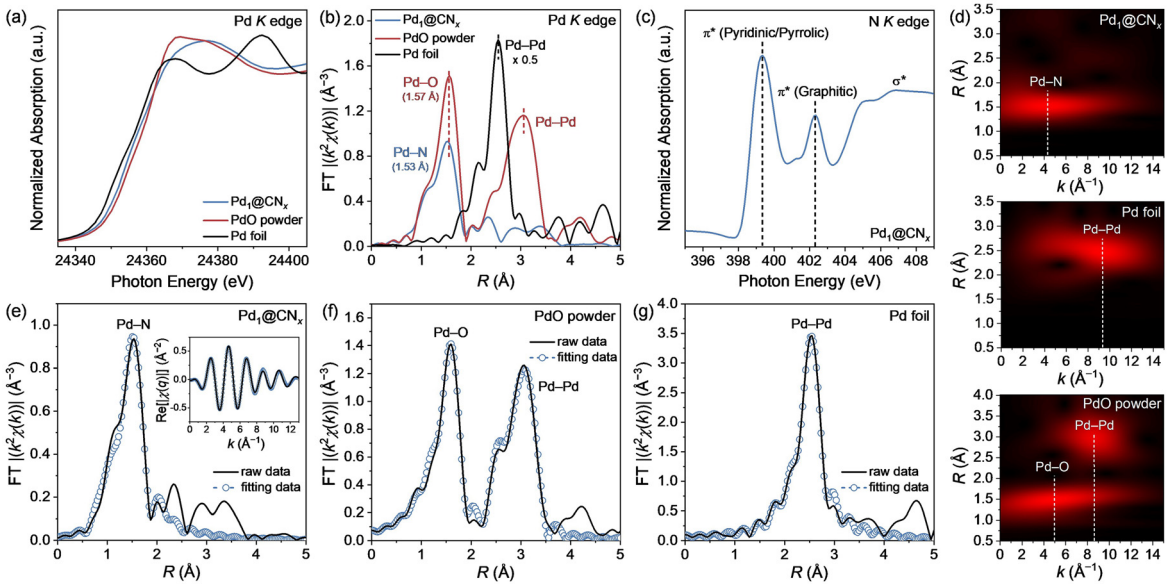

Fig. 2 (a) Normalised Pd *K* edge XANES spectra. (b) Non-phase corrected k^2-weighted Fourier transform EXAFS spectra. (c) Soft XAS N *K* edge spectra. (d) Corresponding WT-EXAFS curves. EXAFS fitting data for (e) 1.32-Pd_1@CN_x, (f) PdO powder, and (g) Pd foil.

rected peaks near 1.53 Å, corresponding to the Pd–N interatomic distance. This suggests primary bonding of Pd atoms with N atoms in the CN_x support with no apparent Pd–Pd bonding observed. In the case of PdO powder, the Pd–O peak was observed near 1.57 Å, at a slightly longer distance than the Pd–N bond in 1.32-Pd_1@CN_x. Finally, intense Fourier transform features peaks are observed above 2.5 Å, indicating the presence of Pd–Pd interatomic distances for both PdO and Pd foil, which are not detected in 1.32-Pd_1@CN_x.

The structural characteristics of surrounding nitrogen were examined by measuring the N *K* edge for 1.32-Pd_1@CN_x (Fig. 2c). Strong peaks near 399 eV were observed in 1.32-Pd_1@CN_x, indicating the electronic transition from N 1s orbital to the π* transition of pyrrolic and pyridinic nitrogen originating from the CN_x support. Notably, the peak intensity of graphitic nitrogen is weaker than pyrrolic/pyridinic nitrogen due to the preliminary nitrogen form in CN_x being pyridinic with unpaired electrons.

Quantitative values from measured EXAFS data, such as interatomic distance, Debye–Waller factor, and coordination number, obtained through EXAFS fitting analysis, are summarised in Table S1. In 1.32-Pd_1@CN_x, the coordination number for the Pd–N bond is 4, consistent with the nature of SACs with an $M–N_4$ structure. In the wavelet-transformed EXAFS (WT-EXAFS) data in Fig. 2d, the prominent maximum is observed around 4.2 $Å^{-1}$ in *k* space, indicating Pd–N bond. The analysis demonstrated that the Pd atoms in 1.32-Pd_1@CN_x are predominantly surrounded by N atoms, aligning with the EXAFS data. In the case of PdO powder and Pd foil, the maxima region in *k* space are present at 8–10 $Å^{-1}$, implying the existence of Pd–Pd bonds in these samples. However, it must be noted that XAS provides averaged information over all Pd sites, and the high synthesis temperature combined with the intrinsic defects of the CN_x substrate may introduce some heterogeneity in Pd coordination. Nonetheless, XANES and EXAFS analyses indicate predominantly atomically dispersed Pd–N species, though complete homogeneity cannot be ensured.

Catalytic performance of the Pd-based catalysts

To optimise the reaction parameters for the photocatalytic Ullmann homocoupling, iodobenzene was employed as a model substrate (Table 2). The choice of base and solvent significantly impacted reaction efficiency, with trends explained by base strength and solvation effects. Specifically, an array of bases was initially examined (entries 1–9). Under benchmark conditions employing 0.67-Pd_1@CN_x, methanol (MeOH), and 1 M aqueous NaOH, the reaction yielded a TOF of 1.80 h^{-1} (entry 1). While NaOH, as a strong base, efficiently deprotonates intermediate species, its inherent nucleophilicity induces side reactions, reducing the overall efficiency. At the other end of the spectrum, Na_2CO_3 (entry 2, TOF = 1.21 h^{-1}), Cs_2CO_3 (entry 3, TOF = 1.29 h^{-1}), and K_2CO_3 (entry 4, TOF = 0.59 h^{-1}), despite their low nucleophilicity, produced suboptimal TOFs, likely due to their weak basicity. K_3PO_4 (entry 5) emerged as the most effective base, achieving a TOF of 1.85 h^{-1}, minimising side reactions while ensuring efficient deprotonation. Finally, organic bases proved unsuitable, consistently yielding low TOFs (entries 6–9). Considering solvent selection, the polar protic nature of methanol (entry 5) allowed it to solvate the base and stabilise charged intermediate species through hydrogen bonding.[31] In contrast, isopropanol (i-PrOH), acetonitrile (MeCN), and dimethylformamide (DMF) all resulted in lower TOFs (entries 10–12). In particular, i-PrOH

Table 2 Ullmann homocoupling of iodobenzene catalysed by Pd catalyst.

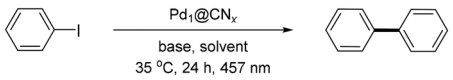

Entry	Base	Base equiv.	Solvent	Conversion (%)	TOF (h^{-1})
1	$NaOH_{aq}$ (1 M)	1	MeOH	76	1.80
2	Na_2CO_3	1	MeOH	44	1.21
3	Cs_2CO_3	1	MeOH	49	1.29
4	K_2CO_3	1	MeOH	26	0.59
5	K_3PO_4	1	MeOH	59	1.85
6	i-Pr_2NH	1	MeOH	9	0.46
7	Bu_2NH	1	MeOH	21	0.24
8	Et_3N	1	MeOH	26	0.25
9	DIPEA	1	MeOH	21	0.38
10	K_3PO_4	1	i-PrOH	33	0.22
11	K_3PO_4	1	MeCN	0	0
12	K_3PO_4	1	DMF	0	0
13	K_3PO_4	2	MeOH	99	2.65
14[a]	K_3PO_4	2	MeOH	99	1.56

Unless indicated otherwise, the reaction conditions were 0.67-$Pd_1@CN_x$ (5 mg), iodobenzene (0.1 mmol), base (0.1–0.2 mmol), and solvent (2 mL). [a] Catalyst amount increased to 7.5 mg. TOF: $mmol_{product}\ mmol_{Pd}^{-1}\ h^{-1}$.

promoted the competitive dehalogenation reaction, decreasing the coupling reaction efficiency.

Doubling the equivalents of K_3PO_4 in MeOH (entry 13) resulted in a TOF of 2.65 h^{-1}. This increase in K_3PO_4 concentration likely enhanced deprotonation efficiency, without introducing significant nucleophilic side reactions. Further investigations revealed that increasing the catalyst amount (entry 14) led to a reduction in TOF. Control experiments (Table S2) confirmed the importance of light (no reaction in its absence), metal catalyst (no biphenyl formation using bare CN_x), and base (traces in its absence).

To assess the effect of Pd loading on catalytic performance, $Pd_1@CN_x$ catalysts with varying Pd contents were tested under the optimised reaction conditions (Fig. 3a). Switching from the lower-loading 0.43-$Pd_1@CN_x$ (TOF of 2.25 h^{-1}) to 0.67-$Pd_1@CN_x$ improved the TOF (2.65 h^{-1}), likely due to a greater number of active Pd single-atom sites facilitating higher catalytic turnover. However, when 1.32-$Pd_1@CN_x$ was employed, the TOF dropped significantly to 1.44 h^{-1}, suggesting that beyond an optimal loading, additional Pd does not enhance catalytic activity proportionally.

Ensuring stability in heterogeneous catalysis is key to minimising performance fluctuations across multiple reaction runs. To assess this within our catalytic protocol, the reaction kinetics were monitored over 24 h (Fig. 3b). Increasing product formation was observed for the first 14 h to a TOF value of 3.79 h^{-1}, whereupon a plateau was reached, and only marginal improvements were observed for the remaining 10 h. Notably, this TOF, to the best of our knowledge, outperformed previous photocatalytic Ullmann homocouplings (Table S3). The durability of the catalyst was further investigated over three successive runs by filtering, washing, drying, and reusing it. Recycling was performed at low conversion (<40%) to avoid operating in a reactant-limited regime (Fig. 3c), followed by a hot filtration test under identical conditions (Fig. S2). After rapid removal of the catalyst, metal-free CN_x photocatalyst was added to the filtrate and maintained under the same conditions. No further biphenyl formation was observed, confirming the absence of catalytically active Pd species in solution. The recovered catalyst was reused in consecutive reactions with comparable activity, confirming its recyclability and the heterogeneous nature of the catalysis. Additionally, recycling at full conversion was performed to assess stability and structural integrity under prolonged operating conditions (Fig. 3d). The catalyst retained high activity, exhibiting only a slight decrease to 96% of its original performance. Further testament to the catalyst's stability was provided by a battery of characterisation techniques performed after the third reaction cycle (Fig. S3). XRD and BET measurements revealed no significant alterations in the catalyst structure, surface area, or porosity. TEM analysis confirmed the absence of metal clusters, demonstrating that metal aggregation did not occur during catalysis. Finally, ICP-OES analysis of the powdered catalyst showed no leaching of Pd during the reactions.

With a reaction profile and the optimal reaction conditions established (Table 2, entry 13), we next sought to expand the substrate scope of our 0.67-$Pd_1@CN_x$ catalyst to aryl halides possessing a variety of functional groups (Scheme S1). Initially, we examined the coupling efficiency of different halobenzenes. The poor leaving group nature of chlorobenzene rendered it inactive for this transformation. However, both iodobenzene and bromobenzene successfully furnished biphenyl **1** with TOFs of 2.65 and 2.25 h^{-1}, respectively. Steric hindrance was also detrimental to coupling efficiency. In comparison to *p*-biaryl **1a**, sterically demanding aryl halides led to decreased TOFs for *m*-biaryl **1b** and *o*-biaryl **1c**.

Further investigations into the substrate scope revealed distinct trends based on the electronic nature of the aryl halides. A marked preference for aryl iodides bearing electron-donating groups was observed, as demonstrated by the 4.96 and 5.10 h^{-1} TOFs achieved with compounds **1a** and **1d**, respectively. Conversely, aryl halides with electron-withdrawing substituents delivered more modest TOFs, reaching up to 2.98 h^{-1} for **1e**. The TOFs declined further for the more strongly deactivated dihalobiphenyls **1f** (2.45 h^{-1}) and **1g** (2.71 h^{-1}), consistent with the diminished electron density of these substrates. This trend is attributed to the substrate-dependent susceptibility of the C–I bond to reductive cleavage: aryl iodides bearing strongly electron-withdrawing groups undergo more facile bond dissociation, due to electron transfer from the carbon nitride support, thereby promoting dehalogenation. In contrast, inactive substrates bearing electron-donating groups exhibit less efficient C–I bond activation, favouring the desired coupling pathway.

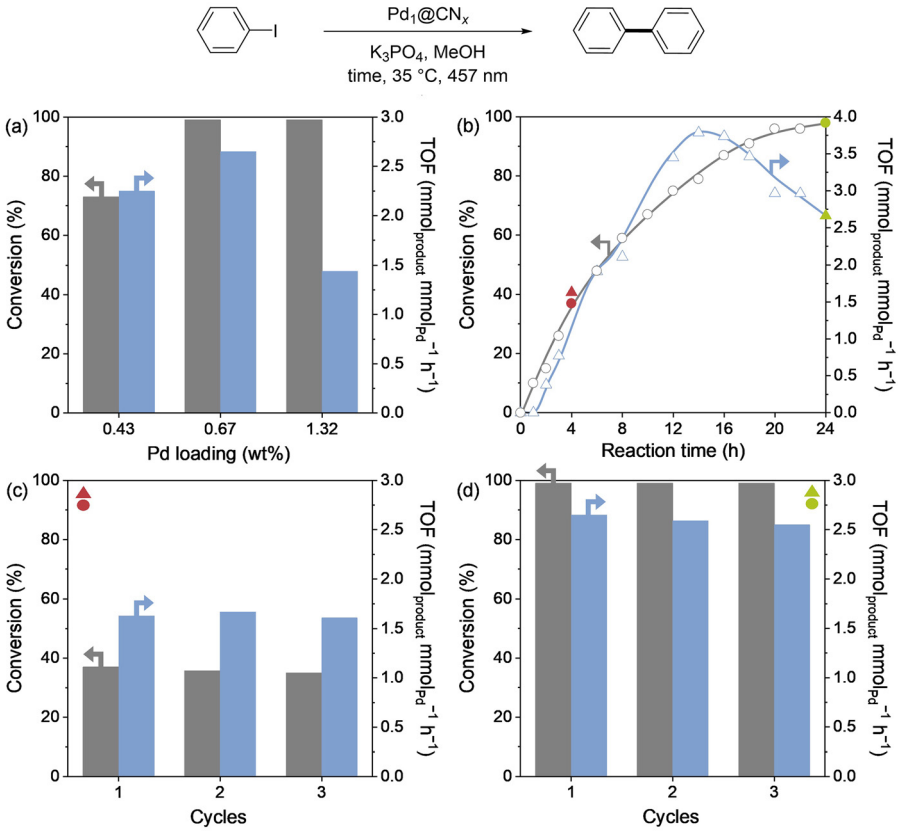

Fig. 3 (a) Pd loading effect, (b) kinetic study, (c) recycling experiments at a conversion level <40%, and (d) recycling experiments at 99% conversion for the photocatalytic Ullmann-type C–C homocoupling reaction. Unless indicated otherwise, the reaction conditions were 0.67-Pd_1@CN_x (5 mg), iodobenzene (0.1 mmol), K_3PO_4 (0.2 mmol), and MeOH (2 mL). For recycling studies, reactions were stopped after 4 h for low conversion and after 24 h for full conversion.

Next, the catalyst compatibility with heteroaromatic halides was explored. These substrates generally exhibit lower reactivity in coupling reactions. In line with this trend, our 0.67-Pd_1@CN_x catalyst delivered bipyridine **1h** in a modest 1.59 h^{-1} TOF. Despite the limited TOF, this result highlights the catalyst's versatility in accommodating even challenging, less reactive aryl halides.

Finally, we successfully utilised the catalyst for the synthesis of hetero-coupled aryl halides (**1i–1m**), achieving TOFs of up to 1.79 h^{-1} for **1l**. Notably, the cross-coupled products showed similar selectivity to the homocoupled products of the unactivated aryl iodides. In contrast, activated aryl halides exhibited significantly lower selectivity for the corresponding homocoupled products, consistent with their limited reactivity during the homocoupling studies.

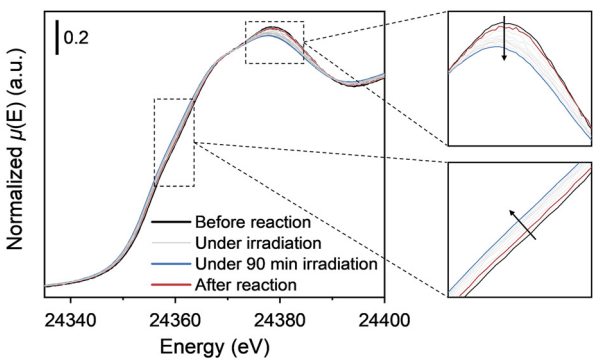

Fig. 4 Pd *K* edge XAS spectra acquired under reaction conditions. The black curve refers to the initial 0.67-Pd_1@CN_x sample in dark conditions, the series of grey curves to irradiation with λ = 457 nm at increasing times up to 90 minutes (blue curve), and the red curve to the final state in dark after reaction.

Mechanistic investigations

To study possible changes in the electronic properties of the metal active site and its stability, XAS measurements were performed under reaction conditions. As can be seen in Fig. 4, upon irradiating the sample at 457 nm under reaction conditions, a progressive reduction in the white line intensity and a shift of the edge position to lower energies (left) are observed (grey curves). The transient phase lasts about 30 minutes, after which a photo-stationary state is reached. This suggests a decrease in the Pd site oxidation state and a change in its coordination. When visible-light irradiation is suspended, as evident from comparing the black and red curves, the system

reverts to its initial state with 4-fold coordination and higher oxidation state, which further corroborate the stability of the catalytic system. The light-induced changes in Pd coordination observed under photocatalytic conditions are consistent with previous studies on SACs, where photoexcitation has been shown to alter the metal's oxidation state and coordination environment,[32] demonstrating how light can uniquely modulate the structural dynamics, activity, and stability of SACs. In our system, which operates without strong bases or homogeneous ligands, illumination is the primary factor driving modifications in the Pd site structure. This behaviour aligns with C–C coupling studies on SACs performed under thermal conditions, where bases and solvents were found to exert only minor effects on the electronic properties of the metal centres.[33,34]

Based on the experimental insights, we considered a Pd atom with a +2 oxidation state and a 4-fold coordination in the triazine cavity of CN_x (Fig. 5a), in accordance with previous studies.[35] More specifically, we recently demonstrated, using X-ray spectroscopy, infrared spectroscopy of probe molecules, and quantum chemical simulations, that during the synthesis of CN_x-based SACs, a Ni atom assumes a four-fold coordination to the matrix.[35] Similarly, in a Pd-based covalent organic framework, we observed that the metal atom is stabilised when occupying a similar cavity.[36] Based on these observations, the choice of the simulated Pd-SAC model is considered reasonable. We modelled the Ullmann-type C–C homocoupling of iodobenzene (RI) to biphenyl (BP) (Fig. 5b). The Pd atom is coordinated to four nitrogen atoms with an average bond length of 2.11 Å (Fig. S4a), where the Pd atom donates $+0.9|e|$ to the CN_x support, as quantified by atomic charge analysis according to the Quantum Theory of Atoms In Molecules (QTAIM), by using Henkelman's algorithm.[37] The 4-fold coordination renders the Pd atom weakly reactive, and a perturbation of its local geometry is needed to make it able to promote the reaction. We hypothesised that $Pd_1@CN_x$ undergoes a low-energy photoexcitation of +1.79 eV, which corresponds to a sub-gap transition enabled by Pd-induced states within the CN_x (*ca.* 2.1 eV).[38] This excitation redistributes electron density around the Pd atom, leading to a calculated contraction of the average Pd–N bond length from 2.11 Å to 1.98 Å. This contraction is well within the range observed for metal centres undergoing changes in oxidation/coordination (*ca.* 0.1–0.15 Å) or for different adsorption geometries in $Pd_1@CN_x$ systems.[34,39]

The overall reaction for the Ullmann homocoupling process is exergonic ($\Delta G = -1.98$ eV) and it consumes two iodobenzene (RI) molecules to release biphenyl (BP) and two iodine ions

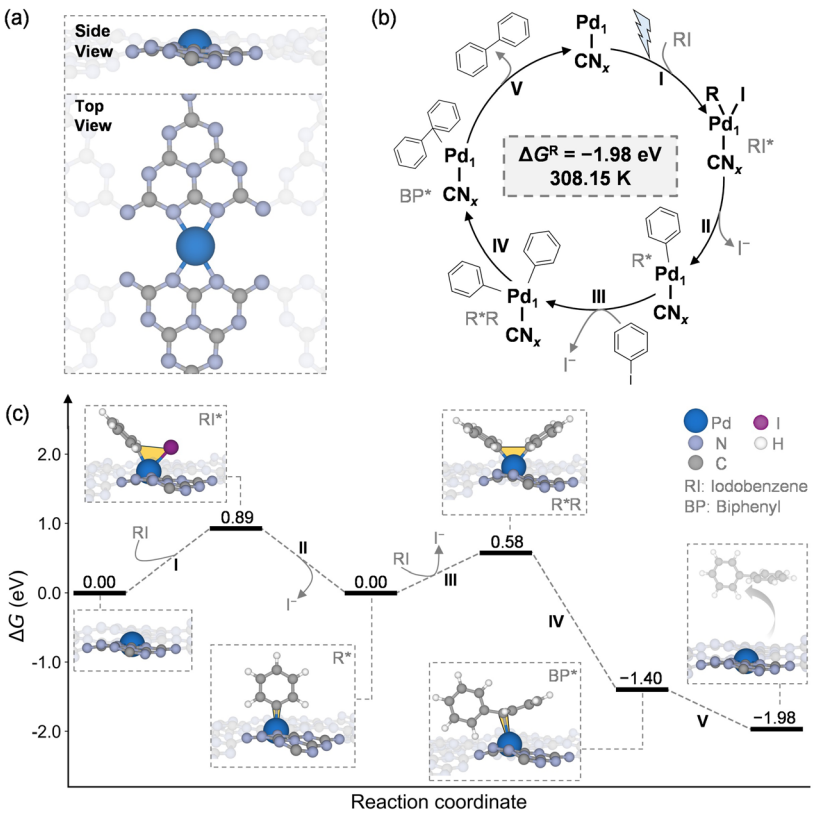

Fig. 5 (a) Side and top views of the atomistic structure of a Pd atom anchored in the triazine pore of CN_x, (b) mechanistic cycle for the Ullmann-type C–C homocoupling of iodobenzene to obtain biphenyl on the $Pd_1@CN_x$ catalyst, and (c) corresponding Gibbs free energy profile. Grey, blue, light purple, purple, and white balls correspond to carbon, palladium, nitrogen, iodine, and hydrogen atoms, respectively. The Roman numbers indicate each elementary step of the process.

($2RI \rightarrow BP + 2I^-$). The proposed mechanism involves the following elementary steps:

$$RI + * \rightarrow RI^* \quad (1)$$

$$RI^* \rightarrow R^* + I^- \quad (2)$$

$$R^* + RI \rightarrow R^*R + I^- \quad (3)$$

$$R^*R \rightarrow BP^* \quad (4)$$

$$BP^* \rightarrow BP + * \quad (5)$$

The first step involves the adsorption of the reactant RI to the single metal site (*), to obtain an adsorbed species of the type RI*, with calculated Pd–C and Pd–I distances equal to 2.09 Å and 2.58 Å respectively, compatible with activated intermediates. This process is endergonic and has an energetic cost of ΔG = +0.89 eV (Fig. 5c, **I**). Indeed, this activation step facilitates the formation of the reaction intermediate (R*), and an iodine ion is released in a favourable process (ΔG = −0.89 eV) (Fig. 5c, **II**). The formation of R* implies a reduction of the Pd–C bond length from 2.09 Å to 1.95 Å, in line with the qualitative description of the bond order conservation principle. To prove that the R* intermediate is the most stable isomer that can be formed when iodobenzene reacts with the catalyst, we simulated other possible isomers (Fig. S5), and we found that indeed this isomer is energetically the most favourable. In the third step, the R* intermediate reacts with a second iodobenzene molecule to form the R*R intermediate. This transformation is endergonic, requiring an energy input of approximately +0.58 eV, and represents a selectivity-controlling stage in the reaction pathway. In the R*R intermediate, the two phenyl groups remain bonded to the Pd with a bond length of 2.05 Å, while the Pd–N bond length increases from 1.98 Å in the R* intermediate to 2.04 Å, and the second iodine ion is released (Fig. 5c, **III**). The subsequent step entails the rearrangement of the two phenyl groups on the Pd@CN_x, leading to the formation of the fourth intermediate BP*, which resembles a biphenyl molecule in the gas phase (Fig. 5c, **IV**). The process is highly exergonic, ΔG = −1.98 eV, and only one carbon from the likely-biphenyl molecule is bonded to the Pd atom with a bond length of 2.50 Å. Within the fourth step, the Pd–N bond length decreases from 2.04 Å in the R*R intermediate to 1.99 Å. The last step is also exergonic, ΔG = −0.58 eV, and involves the release of the biphenyl molecule and the free catalyst (*). Notably, during the reaction, the metal atom changes its coordination to bind reaction intermediates before recovering its initial 4-fold coordination in the triazine cavity of CN_x, in line with the *operando* XAS investigations. Fig. 5c shows the Gibbs free energy profile calculated at T = 308.15 K. Specific bond distances for each intermediate and the catalysts are reported in Fig. S4, whereas the calculated zero-point energy and entropy of the gas-phase molecules and each intermediate are provided in Table S4.

Techno-economic and sustainability assessment

To assess their techno-economic and environmental performance, our SAC (Pd_1@CN_x, as employed in Table 2, entry 13) and a reported nanoparticle-based system (Pd_{NP}@CN_x) were benchmarked against a representative homogeneous protocol through techno-economic analysis (TEA) and life-cycle assessment (LCA) (Fig. 6, Fig. S6–S13, and Tables S5–S7). The homogeneous and heterogeneous systems were comparatively evaluated across two key economic indicators and five major sustainability metrics, including raw material cost, energy consumption, CO_2 emissions, water consumption, carcinogenic toxicity, fine particulate matter formation, and ocean acidification. The Pd_1@CN_x catalyst exhibited substantial improvements across all sustainability parameters relative to the homogeneous counterpart, achieving reductions of 64% in water consumption, 61% in carcinogenic toxicity, 65% in particulate matter formation, and 64% in ocean acidification. Notably, raw material expenses were reduced by 87% owing to the high cost of the $[Au_2(dppm)_2]Cl_2$ catalyst in the homogeneous system. Despite these clear sustainability advantages, the homogeneous protocol displayed higher energy efficiency, primarily due to the multi-step and energy-intensive synthesis of heterogeneous catalysts. Following this comparison, the study focuses exclusively on the heterogeneous systems, with particular emphasis on the comparative techno-economic and environmental evaluation of Pd_1@CN_x and the literature-reported Pd_{NP}@CN_x.

Initially, a TEA was conducted, as illustrated in Fig. 7a and detailed in Tables S8 and S9. A substantial reduction in raw material costs was observed for Pd_1@CN_x compared to Pd_{NP}@CN_x, resulting in a decrease from 193.0 to 37.1 € $g_{product}^{-1}$ $year^{-1}$. The catalyst production cost and solvent expenses were identified as the major contributors to this cost cut. Annual operational costs (OpEx), evaluated across seven cost categories including raw materials, labor, maintenance, utilities, operating charges, lab overhead, and other expenses (Fig. 7b and Tables S10 and S11), also decreased by nearly 70%, while the total energy consumption (Fig. 7c and detailed in Table S12) was reduced by 62% when Pd_1@CN_x was used instead of Pd_{NP}@CN_x.

The environmental impacts of the catalytic processes employing Pd_1@CN_x and Pd_{NP}@CN_x were evaluated through an LCA. In the initial phase of the analysis, the two reactions were compared across key environmental indicators, including carbon emissions (kg CO_2 equiv. $g_{product}^{-1}$) and water consumption (m^3 $g_{product}^{-1}$). By exploiting Pd_1@CN_x in the reaction, CO_2 emissions were mitigated from 58.6 to 19.2 kg CO_2 equiv. $g_{product}^{-1}$, representing a 67% reduction compared to the nanoparticle-based protocol (Fig. 8a and Tables S13 and S14). This improvement was primarily driven by the more sustainable synthesis of the catalyst (Pd_1@CN_x catalyst), which alone contributed to a cut of 38.9 kg CO_2 equiv. $g_{product}^{-1}$. In addition, the replacement of the dioxane–H_2O mixture (3 : 5 v/v) with methanol had a positive effect on the emissions. In the Pd_{NP}@CN_x system, solvent-related emissions accounted for

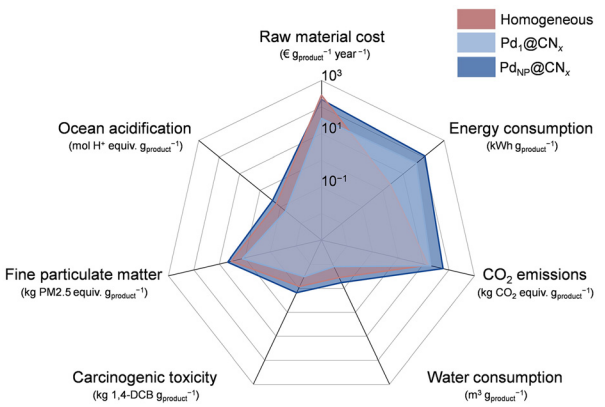

Fig. 6 Comparative evaluation of homogeneous (red) and heterogeneous (blue) systems across key economic and sustainability metrics.

1.1 kg CO_2 equiv. $g_{product}^{-1}$, whereas methanol in the $Pd_1@CN_x$ protocol reduced the emissions to 0.4 kg CO_2 equiv. $g_{product}^{-1}$. Water consumption was also evaluated, showing a 74% reduction under $Pd_1@CN_x$ conditions, decreasing from 4.7 to 1.2 m^3 $g_{product}^{-1}$ (Fig. 8a and Tables S15 and S16). A key factor in this improvement was the lower Pd loading in the $Pd_1@CN_x$ catalyst, which reduced the water required during metal precursor processing from 4.6 to 1.1 m^3 $g_{product}^{-1}$ compared to the nanoparticle-based counterpart.

A broader evaluation was performed to capture aggregated environmental impacts on three major damage categories: human health, ecosystem quality, and critical resources (Fig. 8b and Tables S17 and S18). A reduced overall environmental impact was associated with $Pd_1@CN_x$ conditions relative to the nanoparticle-based system, with damage reductions of 72% in human health, 73% in ecosystem quality, and 68% in resources.

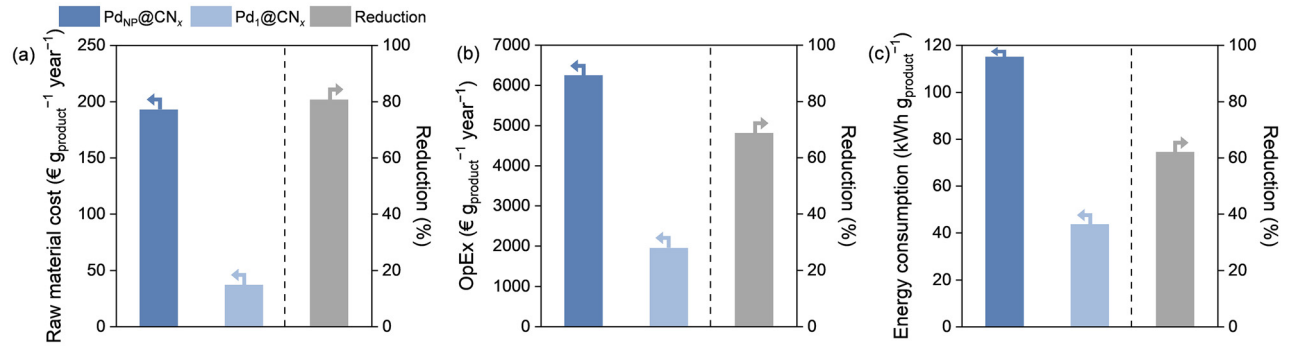

Fig. 7 Techno-economic evaluation of $Pd_1@CN_x$ and $Pd_{NP}@CN_x$ reaction conditions in terms of (a) raw material cost, (b) OpEx, and (c) energy consumption.

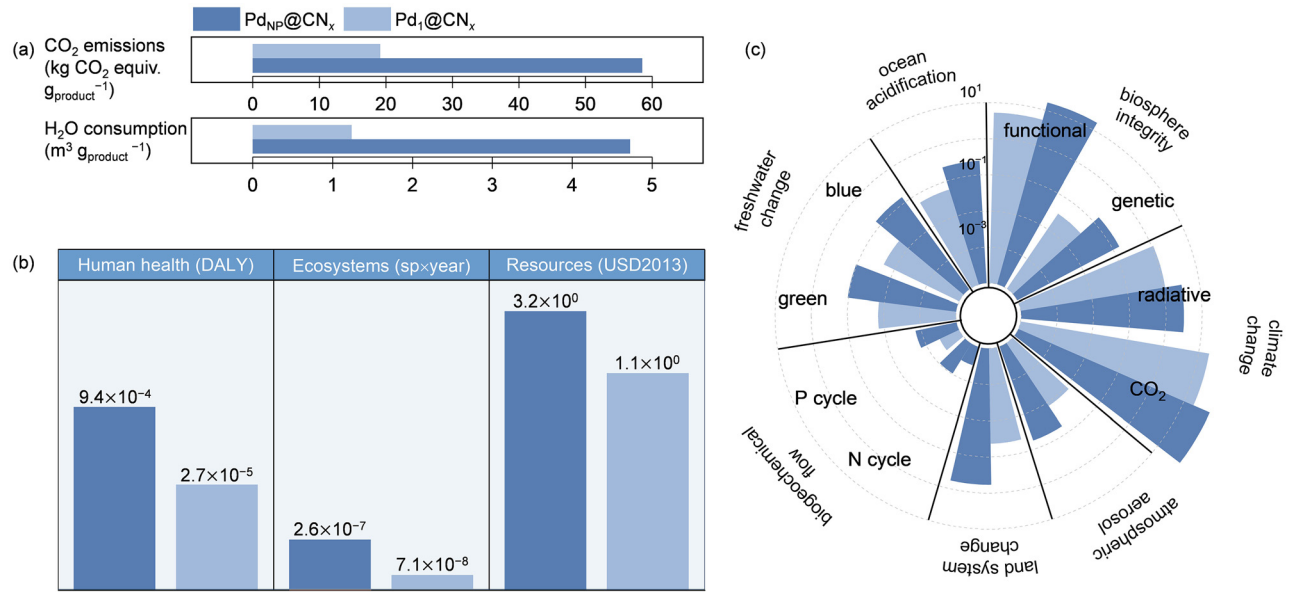

Fig. 8 (a) Environmental impact comparison of $Pd_1@CN_x$ and $Pd_{NP}@CN_x$ reaction conditions in terms of CO_2 emissions and water consumption, (b) endpoint damage categories, and (c) 9 planetary boundaries. Human health impact is expressed in disability-adjusted life years (DALY) and ecosystem quality impact in species lost × years.

Building upon the endpoint analysis, the assessment was further extended to include midpoint level indicators and implemented into a planetary boundary framework (Fig. 8c and detailed in Tables S19 and S20) to characterise individual environmental stressors with greater precision. The impact on ocean acidification was notably reduced under reaction conditions exploiting $Pd_1@CN_x$, from 2.5×10^{-1} to 5.7×10^{-2} mol H^+ equiv. $g_{product}^{-1}$. This outcome was primarily linked to the reduced Pd content and the solvent system employed. Specifically, the use of $Pd_1@CN_x$ catalyst led to significantly lower acidification impact, showing a 78% reduction relative to the $Pd_{NP}@CN_x$ system, decreasing from 2.4×10^{-1} to 5.2×10^{-2} mol H^+ equiv. $g_{product}^{-1}$. Furthermore, the use of methanol in the $Pd_1@CN_x$ protocol resulted in a reduction in the solvent-derived acidification impact from 4.5×10^{-3} to 1.4×10^{-3} mol H^+ equiv. $g_{product}^{-1}$, reflecting its lower acidification potential compared to the dioxane–H_2O system. The genetic and functional biosphere integrities also followed a similar trend and decreased by 79% and 68%, respectively. Moreover, under $Pd_1@CN_x$ conditions, the impact on climate change was reduced by 67% and 65%, considering the effects of radiative forcing and carbon emissions, respectively. Atmospheric aerosol loading is a critical parameter influencing Earth's radiative balance and air quality, thereby playing a pivotal role in human health. The use of $Pd_1@CN_x$ in the catalytic method enhanced process sustainability, reducing atmospheric aerosol impacts by 78%. Land system change, closely associated with deforestation as a primary environmental pressure, was notably mitigated under the $Pd_1@CN_x$ protocol. The impact in this category was reduced by 93%, corresponding to a land use saving of 5.5×10^{-1} m^2 crop equiv. $g_{product}^{-1}$ compared to the $Pd_{NP}@CN_x$ conditions. Further reductions were observed in the biogeochemical flows, where the use of $Pd_1@CN_x$ lowered the impacts on phosphorus and nitrogen cycles by 73% and 64%, respectively. Lastly, the impacts on green and blue waters were investigated in the context of freshwater change. The conditions with $Pd_1@CN_x$ exhibited a much greener performance for both freshwater impact categories, and the impacts were minimised by 87% and 86%, respectively.

We next examined catalyst synthesis routes, quantifying carbon emissions to assess the environmental burden associated with the preparation of the catalytic material (Fig. S14 and Tables S21–S26). Also in this case, the synthesis of the nanoparticle-based catalyst led to much greater carbon emissions. In comparison, the preparation of the $Pd_1@CN_x$ catalyst resulted in a 69% reduction in carbon emissions, highlighting the environmental advantages of the protocol. One of the major reasons for this reduction was the energy-intensive synthetic protocol of the reported $Pd_{NP}@CN_x$ catalyst, wherein 84% of the total carbon emissions originated from energy consumption. This high energy demand was further amplified by the low catalyst mass yield (*ca.* 50%), which increased the energy input required per gram of catalyst synthesised. Another notable contributor to the elevated carbon emissions was the selection of the Pd precursor (K_2PdCl_6), which accounted for 13% of the total emissions owing to the carbon-intensive production of Pd metal for precursor synthesis. In contrast, the $Pd_1@CN_x$ synthesis protocol significantly reduced carbon emissions by addressing the energy-intensive characteristics of the nanoparticle-based route, achieving a 65% decrease in energy consumption. Finally, $Pd_{NP}@CN_x$ catalyst required a higher Pd precursor consumption (*ca.* 0.7 $g_{precursor}$ $g_{catalyst}^{-1}$), which increased the resource intensity of the process. In contrast, the $Pd_1@CN_x$ catalyst led to a 93% reduction in precursor-related consumption. The results corroborated the advantage of SACs in minimising the use of critical raw materials, in contrast to nanoparticle systems where a larger fraction of the metal is required and remains inactive in the catalytic process.

Conclusion

We developed a family of $Pd_1@CN_x$ catalysts with tuneable Pd loadings between 0.43–1.32 wt%. Advanced spectroscopy (XPS and XAS) unambiguously confirmed atomically dispersed Pd in a $Pd–N_4$ coordination environment without Pd–Pd contributions assigned to metal clusters and nanoparticles. In the photocatalytic Ullmann homocoupling of aryl halides, the optimal catalyst (0.67-$Pd_1@CN_x$) achieved a TOF of 2.65 h^{-1} under visible light, with reaction kinetics reaching 3.79 h^{-1} after 14 h, which surpass previously reported photocatalytic systems. The catalyst also exhibited good stability, retaining 96% activity after three cycles, without evidence of aggregation or Pd leaching. DFT calculations and *operando* XAS revealed a light-induced Pd^{2+} coordination dynamics that enables substrate activation, consistent with a low-energy barrier ($\Delta G^{\ddagger} \approx +0.58$ eV) for the selectivity-controlling step. From a techno-economic perspective, the $Pd_1@CN_x$ protocol reduced raw material costs from 193.0 to 37.1 € $g_{product}^{-1}$ $year^{-1}$ and operating expenses by *ca.* 70% relative to Pd nanoparticle benchmarks. Energy consumption was also lowered by 62%, while life cycle assessment showed *ca.* 70% less CO_2 emissions. Collectively, these results demonstrate that Pd SACs not only unlock superior photocatalytic Ullmann couplings but also establish a scalable and environmentally sustainable route to C–C bond formation.

Materials and methods

Catalyst preparation

The Pd single atoms anchored on CN_x catalysts were prepared according to a modified literature procedure.[40] Cyanamide (3 g) and the appropriate amount of K_2PdCl_4 were added to a 40% aqueous dispersion of 12 nm SiO_2 particles (7.5 g). Specifically, 30 mg (0.09 mmol), 52 mg (0.16 mmol), and 85 mg (0.26 mmol) of K_2PdCl_4 were used to prepare the 0.43 wt%, 0.67 wt%, and 1.32 wt% $Pd_1@CN_x$ catalysts, respectively. The suspension was stirred at 80 °C for 16 h, leading to complete water evaporation. The resultant solid mixture was heated to 550 °C at a rate of 2.2 °C min^{-1} and maintained at that temperature for 4 h. The obtained orange powder was briefly ground

and washed with an $(NH_4)HF_2$ solution (12 g in 50 mL of water) for 24 h to remove the silica template. The solid was collected by filtration, washed with water (3 × 100 mL) and ethanol (100 mL), and dried in an oven at 65 °C overnight to yield 1.5 g of the desired $Pd_1@CN_x$. Reference CN_x was prepared similarly but without the addition of metal precursor (K_2PdCl_4).

Catalyst characterisation

Inductively coupled plasma optical emission spectroscopy (ICP-OES) was conducted on a PerkinElmer Optima 8300 ICP-OES spectrometer to determine the Pd content of $Pd_1@CN_x$. The elemental composition of samples was determined using a Vario MICRO Elemental Analyzer through combustion analysis at temperatures exceeding 1000 °C in an oxygen-rich environment. Powder X-ray diffraction (XRD) was performed on a Bruker D2 Phaser diffractometer equipped with a Cu Kα radiation source (λ = 1.54 Å), using a 2θ step size of 0.016° and a counting time of 0.4 s per step. Nitrogen physisorption measurements were performed on a Micromeritics ASAP 2020 instrument at −196 °C after degassing the samples at 150 °C for 24 h. The specific surface areas were calculated by applying the Brunauer–Emmett–Teller (BET) model to the adsorption branch in the p/p_0 range from 0.05 to 0.30. Transmission electron microscopy (TEM) studies were conducted using a Philips CM200 FEG instrument operated at 200 kV equipped with a cold field emission gun. High-resolution TEM (HR-TEM) studies were performed using the GrandARM300F (JEOL, Japan) with a cold field emission gun operated at 300 kV. Aberration correction of the image-forming as well as of the probe-forming lenses enabled sub-Å resolution. For X-ray photoelectron spectroscopy (XPS) measurements, the powdered catalyst was distributed and pressed onto a double-sided carbon adhesive tape, which was fixed on a flag-style sample holder and then introduced into the ultrahigh-vacuum analysis chamber *via* a load-lock. The carbon tape was fully covered to ensure that no additional signal contributions were detected. The analysis chamber was equipped with a dual anode X-ray source (XR50, Specs) and a hemispherical electron energy analyser (Argus CU, Scienta Omicron). The XP spectra of the catalyst samples were acquired with Al Kα radiation (1486.7 eV) at normal emission. For the Pd 3d, C 1s, and N 1s detail spectra, the analyser pass energy was set to 50 eV. Charging effects were considered by relating the BE scale to the C 1s signal of the aromatic carbon at 284.7 eV. X-ray absorption spectroscopy (XAS) measurements for the Pd *K* edge were carried out at the Pohang Light Source-II (PLS-II) 8C Nanoprobe XAFS beamline (BL8C). A double crystal monochromator with Si (111) crystal was used to deliver a monochromatic X-ray beam. The slits used in all measurements had an aperture of 0.5 mm (vertical) × 1 mm (horizontal). The measurements were performed at the Pd *K* edge in transmission mode using gas ionisation chambers as the detectors.

Photocatalytic experiments

A 4 mL glass vial was charged with catalyst (5–7.5 mg), the appropriate aryl halide (0.1 mmol), base (0.1–0.2 mmol), and solvent (2 mL), and sealed with a silicone septum. The experiments were conducted in a PhotoCube™ reactor (ThalesNano Inc.) under visible light irradiation (λ = 457 nm) for 24 h at 35 °C. For the reaction optimisation, the crude was filtered through a Nylon syringe filter (0.45 μm) after reaction completion and analysed by high-performance liquid chromatography (HPLC). Aliquots of 100 μL from the reaction mixtures were diluted with 1.5 mL of MeCN and injected into an Agilent 1200 chromatograph (G1315D UV detector at λ = 210 nm). The stationary phase used was a C18 HypersilGOLD 5 μm 175 Å column (Thermo Scientific) and the eluent was a 60 : 40 mixture of MeCN/H_2O (flow rate: 0.7 mL min^{-1} at 40 °C). Conversion and TOF were determined after HPLC calibration with commercial standards. Specifically, the amount of product (mmol), quantified by HPLC, was used to calculate the TOF according to the following equation, where $mmol_{Pd}$ is the Pd content in the catalyst (mmol) and h the reaction time:

$$\mathrm{TOF}\left(\mathrm{h}^{-1}\right) = \frac{\mathrm{mmol}_{\mathrm{product}}}{\mathrm{mmol}_{\mathrm{Pd}} \times \mathrm{h}}$$

For recycling studies, after reaction completion, the catalyst was separated by filtration, washed with water (15 mL) and methanol (15 mL), dried in an oven at 60 °C, and reused in the next cycle. After the recycling tests, the Pd loading of the recovered catalyst was detected by ICP-OES to be 0.67 wt%. For recycling at low conversion, the reaction was stopped after 4 h. To investigate Pd leaching, a hot filtration test was performed under the same conditions. After rapid catalyst removal, metal-free CN_x (5 mg) and K_3PO_4 (0.2 mmol) were added to the filtrate, and the mixture was maintained under identical conditions. To investigate the generality of the reaction, a substrate scope was conducted using a diverse array of substrates under the optimised conditions. After each reaction, the catalyst was separated by filtration and washed with methanol (15 mL). The solvent was then removed under reduced pressure. The resultant crude mixture was treated with H_2O (10 mL) and extracted with ethyl acetate (3 × 10 mL). The organic phase was dried with $MgSO_4$, filtered, concentrated under reduced pressure, and re-dissolved in $CDCl_3$. Dibromomethane or 2,2,2-trifluoroethanol (0.1 mmol) was added as an external standard and the mixture was analysed by means of NMR spectroscopy. Yields determined by ^1H or ^{19}F NMR spectroscopy.

DFT calculations

Spin-polarised DFT calculations were performed with the VASP code,[41–43] using the generalised gradient approximation, as implemented in the Perdew–Burke–Ernzerhof (PBE) functional.[44] Dispersion forces have been included according to Grimme's D3 parametrisation.[45] The valence electrons have been expanded on a set of plane waves with a kinetic energy cutoff of 450 eV, whereas the core electrons were treated with the projector augmented wave approach (PAW).[46,47] The threshold criteria for electronic and ionic loops were set to 1×10^{-6} eV and 1×10^{-2} eV $Å^{-1}$, respectively. The sampling of the reciprocal space was reduced to the gamma point because of

the cell size. Single-point PBE0[48,49] calculations were performed on top of PBE-optimised structures to improve the description of the electronic structure. This strategy allows us to avoid intensive geometry optimisations with hybrid functionals with an acceptable error bar of about 0.1 eV.[50] As a catalyst, we considered a newly elucidated carbon nitride structure, which some of us recently validated through experimental results and DFT simulations.[35] The optimised lattice parameters for the CN_x are: a = 15.593 Å, b = 20.698 Å, γ = 90.2°. Each intermediate's binding energies (ΔE) were calculated with respect to the free molecular species and the catalyst. The Gibbs energies (ΔG) were evaluated by adopting the thermochemistry approach of Nørskov and co-workers, including zero-point energy correction and entropy terms.[51,52] The entropy of adsorbed species and gas-phase molecules was calculated through the harmonic approximation, following the methodology previously reported by some of the authors,[53] and accounting for the reaction temperature (35 °C); the entropy of solid-state species was considered equal to zero.[52] To account for the Pd +2 oxidation state, we simulated all systems with a +2 charge, *e.g.*, $[Pd@CN_x]^{2+}$, following a previous study.[35]

Operando XAS

Pd *K* edge XAS measurements under reaction conditions were performed at the ID24-DCM beamline of the European Synchrotron Radiation Facility (ESRF) in Grenoble, France. The spectra were collected in fluorescence mode, employing a capillary to host the sample in powder form. The capillary was connected to a liquid-flow setup to circulate the reaction solution containing iodobenzene, solvent, and base. The *operando* experiment was conducted under visible light irradiation (λ = 457 nm). Background subtraction, energy alignment, and edge jump normalisation were carried out with the ATHENA software as part of the Demeter suite.[54]

Techno-economic analysis

Techno-economic assessments were conducted using Aspen Plus® V11.[55] The simulations incorporated a stoichiometric reactor model with fractional conversion parameters to accurately reflect the experimentally observed performance of the processes under steady-state conditions. The thermophysical and chemical properties of all components were sourced from integrated databases (APV110, APESV110, and NISTV110)[56] within the software environment. Simulation inputs, including temperature, pressure, and feed streams, were applied identically with experimental operating conditions. In order to compute the total energy consumption of the reactions, electricity was accounted for as a utility input. Cost estimations were determined from real reactor volumes using the Aspen Process Economic Analyzer (APEA). To evaluate raw material costs, the unit prices of the chemical components were obtained from Merck's commercial database.[57]

Life-cycle assessment

Goal and scope definition. Life cycle assessment (LCA) was conducted using SimaPro® V9.5, following a cut-off system model under a cradle-to-gate boundary.[58] To ensure consistency across all evaluated scenarios, the functional unit applied in the LCA was defined as the production of 1 gram of target product. LCA endpoint indicators were employed to assess the overall sustainability profiles of reaction conditions, addressing damage to human health (DALY), ecosystems (species lost × years) and resources (USD 2013).[59] In addition, a detailed comparison was carried out using 11 LCA midpoint categories mapped onto the nine planetary boundaries (9PB), including ocean acidification, genetic and functional biosphere integrities, carbon emissions, radiative forces, atmospheric aerosol loading, land systems changes, phosphorus and nitrogen cycles, and green and blue water changes.[60] Impact assessment to quantify contributions to planetary boundary categories was carried out using ReCiPe 2016 Midpoint (H),[61] ReCiPe 2016 Endpoint (H),[61] and Environmental Footprint 3.1 (EF).[62] The ReCiPe 2016 Midpoint (H) method was employed to evaluate the following categories: (1) climate change *via* global warming potential and ionising radiation; (2) atmospheric aerosol loading *via* fine particulate matter formation; (3) biogeochemical flows *via* freshwater and marine eutrophication; (4) land system change *via* land use; (5) freshwater change *via* ecotoxicity in freshwater and marine compartments; and (6) functional and genetic biosphere integrities *via* carcinogenic toxicity; mineral and fossil resource depletion, terrestrial acidification, and ozone formation impacts, respectively. Additionally, ocean acidification was computed *via* only EF 3.1 methodology.

Inventory analysis. Life cycle inventory data, including material and energy inputs, were obtained from the Ecoinvent v3 database. For materials not available in the database, a retrosynthetic approach was employed to construct representative inventories, as reported in the SI. Process-specific energy consumption values were extracted from Aspen Plus® V11.[55]

Author contributions

A. M. was responsible for catalyst preparation and characterisation, collected catalytic data, and carried out *operando* XAS experiments. T. A. G. generalised the findings to more reactants. L. A. C. and G. D. L. performed DFT calculations. I. S. K. conducted XAS studies, while M. S. performed XPS studies. M. C. I. conducted techno-economic analysis and life-cycle assessment. N. A. and S. F. J. carried out *operando* XAS experiments. L. M. and E. B. supervised the *operando* XAS studies and L. M. did data analysis. G. V. coordinated and supervised the project. All authors contributed to writing the manuscript and approved its final version.

Conflicts of interest

There are no conflicts to declare.

Data availability

The data that support the findings of this study are available from the corresponding author upon reasonable request.

Supplementary information (SI): additional characterisation and catalytic results of the materials; EXAFS fitting results; additional DFT calculations; TEA and LCA details; and NMR characterisations of the reaction products. See DOI: https://doi.org/10.1039/d5gc04693a.

Acknowledgements

A. M. and N. A. thank financial support from the European Commission under the Horizon Europe's Global Challenges and European Industrial Competitiveness programme ("SusPharma", grant agreement 101057430). T. A. G. gratefully acknowledge financial support from the European Commission through a Marie Skłodowska-Curie Postdoctoral Fellowship ("SOLCAT", grant agreement 101152890). G. V. and L. A. C. thank the European Research Council ("SAC_2.0", grant agreement 101075832) for an ERC Starting Grant. M. C. I. thanks the European Commission's Horizon Europe research and innovation programme for the Marie Skłodowska-Curie doctoral fellowship ("GreenDigiPharma", grant agreement 101073089). G. D. L. and L. M. have received funding from the Italian Ministry of University and Research (MUR) and the European Union – Next Generation EU, Mission 4, Component 1 through the PRIN project "UNDERSAC" (CUP: 2022LRPSTS). The authors thank the European Synchrotron Radiation Facility (ESRF) for allocation of beamtime at the beamline ID24-DCM and Dr Davide Salusso (ESRF) for the support during experiment CH-7183. The authors also kindly acknowledge Xiufang He for support during *operando* XAS experiments, Cinzia Ferrario for TEM analyses, and Grazia Isa Carla Righetti for support with catalytic data not shown in this paper regarding Pd-based catalysts.

References

1 F. Khan, M. Dlugosch, X. Liu and M. G. Banwell, *Acc. Chem. Res.*, 2018, **51**, 1784–1795.
2 X. Gong, J. Wu, Y. Meng, Y. Zhang, L.-W. Ye and C. Zhu, *Green Chem.*, 2019, **21**, 995–999.
3 A. Kamal, V. Srinivasulu, B. N. Seshadri, N. Markandeya, A. Alarifi and N. Shankaraiah, *Green Chem.*, 2012, **14**, 2513.
4 H. Jiang, J. Xu, S. Zhang, H. Cheng, C. Zang and F. Bian, *Catal. Sci. Technol.*, 2021, **11**, 219–229.
5 R. N. Dhital, C. Kamonsatikul, E. Somsook, K. Bobuatong, M. Ehara, S. Karanjit and H. Sakurai, *J. Am. Chem. Soc.*, 2012, **134**, 20250–20253.
6 X. Tian, Y. Guo, W. An, Y.-L. Ren, Y. Qin, C. Niu and X. Zheng, *Nat. Commun.*, 2022, **13**, 6186.
7 L. Zhang, A. Wang, J. T. Miller, X. Liu, X. Yang, W. Wang, L. Li, Y. Huang, C.-Y. Mou and T. Zhang, *ACS Catal.*, 2014, **4**, 1546–1553.
8 A. Wang, J. Li and T. Zhang, *Nat. Rev. Chem.*, 2018, **2**, 65–81.
9 V. B. Saptal, V. Ruta, M. A. Bajada and G. Vilé, *Angew. Chem., Int. Ed.*, 2023, **62**, e202219306.
10 H. B. Kale, A. D. Kute, R. P. Gaikwad, P. Fornasiero, R. Zbořil and M. B. Gawande, *Coord. Chem. Rev.*, 2024, **502**, 215602.
11 X. Cui, W. Li, P. Ryabchuk, K. Junge and M. Beller, *Nat. Catal.*, 2018, **1**, 385–397.
12 L.-H. Xu, W. Liu and K. Liu, *Adv. Funct. Mater.*, 2023, **33**, 2304468.
13 V. Giulimondi, S. Mitchell and J. Pérez-Ramírez, *ACS Catal.*, 2023, **13**, 2981–2997.
14 C. Gao, J. Low, R. Long, T. Kong, J. Zhu and Y. Xiong, *Chem. Rev.*, 2020, **120**, 12175–12216.
15 S. Wu and P. Schmuki, *Adv. Mater.*, 2024, **37**, 2414889.
16 A. Moutsiou, A. Olivati, L. A. Cipriano, A. Sivo, S. M. Collins, Q. M. Ramasse, I. S. Kwon, G. Di Liberto, M. Kanso, R. Wojcieszak, G. Pacchioni, A. Petrozza and G. Vilé, *ACS Catal.*, 2025, **15**, 5601–5613.
17 W. Li, X. Zheng, B. Xu, Y. Yang, Y. Zhang, L. Cai, Z. Wang, Y. Yao, B. Nan, L. Li, X. Wang, X. Feng, M. Antonietti and Z. Chen, *Angew. Chem., Int. Ed.*, 2024, **63**, e202320014.
18 S. Wang, H. Wang and B. König, *J. Am. Chem. Soc.*, 2021, **143**, 15530–15537.
19 A. Savateev, I. Ghosh, B. König and M. Antonietti, *Angew. Chem., Int. Ed.*, 2018, **57**, 15936–15947.
20 G. F. S. R. Rocha, M. A. R. Da Silva, A. Rogolino, G. A. A. Diab, L. F. G. Noleto, M. Antonietti and I. F. Teixeira, *Chem. Soc. Rev.*, 2023, **52**, 4878–4932.
21 M. Gawande, P. Fornasiero and R. Zbořil, *ACS Catal.*, 2020, **10**, 2231–2259.
22 G. Vilé, D. Albani, M. Nachtegaal, Z. Chen, D. Dontsova, M. Antonietti, N. López and J. Pérez-Ramírez, *Angew. Chem., Int. Ed.*, 2015, **54**, 11265–11269.
23 S. Büchele, A. Yakimov, S. M. Collins, A. Ruiz-Ferrando, Z. Chen, E. Willinger, D. M. Kepaptsoglou, Q. M. Ramasse, C. R. Müller, O. V. Safonova, N. López, C. Copéret, J. Pérez-Ramírez and S. Mitchell, *Small*, 2022, **18**, 2202080.
24 L. Jiao, R. Zhang, G. Wan, W. Yang, X. Wan, H. Zhou, J. Shui, S.-H. Yu and H.-L. Jiang, *Nat. Commun.*, 2020, **11**, 2831.
25 V. Ruta, A. Sivo, L. Bonetti, M. A. Bajada and G. Vilé, *ACS Appl. Nano Mater.*, 2022, **5**, 14520–14528.
26 A. Sivo, V. Ruta, V. Granata, O. Savateev, M. A. Bajada and G. Vilé, *ACS Sustainable Chem. Eng.*, 2023, **11**, 5284–5292.
27 K. S. Lakhi, D.-H. Park, K. Al-Bahily, W. Cha, B. Viswanathan, J.-H. Choy and A. Vinu, *Chem. Soc. Rev.*, 2017, **46**, 72–101.
28 R. Arrigo, M. E. Schuster, Z. Xie, Y. Yi, G. Wowsnick, L. L. Sun, K. E. Hermann, M. Friedrich, P. Kast, M. Hävecker, A. Knop-Gericke and R. Schlögl, *ACS Catal.*, 2015, **5**, 2740–2753.
29 Z. Chen, E. Vorobyeva, S. Mitchell, E. Fako, M. A. Ortuño, N. López, S. M. Collins, P. A. Midgley, S. Richard, G. Vilé

and J. Pérez-Ramírez, *Nat. Nanotechnol.*, 2018, **13**, 702–707.
30 M. A. Bajada, G. Di Liberto, S. Tosoni, V. Ruta, L. Mino, N. Allasia, A. Sivo, G. Pacchioni and G. Vilé, *Nat. Synth.*, 2023, **2**, 1092–1103.
31 C. Reichardt and T. Welton, *Solvents and Solvent Effects in Organic Chemistry*, Wiley-VCH, Weinheim, 2011.
32 L. Piccolo, P. Afanasiev, F. Morfin, T. Len, C. Dessal, J.-L. Rousset, M. Aouine, F. Bourgain, A. Aguilar-Tapia, O. Proux, Y. Chen, L. Soler and J. Llorca, *ACS Catal.*, 2020, **10**, 12696–12705.
33 M. E. Usteri, G. Giannakakis, A. Bugaev, J. Pérez-Ramírez and S. Mitchell, *ACS Catal.*, 2024, **14**, 12635–12646.
34 G. Giannakakis, M. E. Usteri, A. Bugaev, A. Ruiz-Ferrando, D. Faust Akl, N. López, S. Fantasia, K. Püntener, J. Pérez-Ramírez and S. Mitchell, *ACS Catal.*, 2025, **15**, 284–295.
35 N. Allasia, S. Xu, S. F. Jafri, E. Borfecchia, L. A. Cipriano, G. Terraneo, S. Tosoni, L. Mino, G. Di Liberto, G. Pacchioni and G. Vilé, *Small*, 2025, **21**, e2408286.
36 V. B. Saptal, C. Saetta, A. Laufenböck, M. Sterrer, I. S. Kwon, A. Lucotti, M. Tommasini, O. Tomanec, A. Bakandritsos, G. Di Liberto, G. Pacchioni and G. Vilé, *J. Am. Chem. Soc.*, 2025, **147**, 18524–18540.
37 G. Henkelman, A. Arnaldsson and H. Jónsson, *Comput. Mater. Sci.*, 2006, **36**, 354–360.
38 G. Gao, Y. Jiao, E. R. Wacławik and A. Du, *J. Am. Chem. Soc.*, 2016, **138**, 6292–6297.
39 E. Biasin, T. B. van Driel, K. S. Kjær, A. O. Dohn, M. Christensen, T. Harlang, P. Chabera, Y. Liu, J. Uhlig, M. Pápai, Z. Németh, R. Hartsock, W. Liang, J. Zhang, R. Alonso-Mori, M. Chollet, J. M. Glownia, S. Nelson, D. Sokaras, T. A. Assefa, A. Britz, A. Galler, W. Gawelda, C. Bressler, K. J. Gaffney, H. T. Lemke, K. B. Møller, M. M. Nielsen, V. Sundström, G. Vankó, K. Wärnmark and S. E. Canton, *Phys. Rev. Lett.*, 2016, **117**, 013002.
40 G. Vilé, G. Di Liberto, S. Tosoni, A. Sivo, V. Ruta, M. Nachtegaal, A. H. Clark, S. Agnoli, Y. Zou, A. Savateev, M. Antonietti and G. Pacchioni, *ACS Catal.*, 2022, **12**, 2947–2958.
41 G. Kresse and J. Hafner, *Phys. Rev. B: Condens. Matter Mater. Phys.*, 1993, **47**, 558–561.
42 G. Kresse and J. Hafner, *Phys. Rev. B: Condens. Matter Mater. Phys.*, 1994, **49**, 14251–14269.
43 G. Kresse and J. Furthmüller, *Comput. Mater. Sci.*, 1996, **6**, 15–50.
44 J. P. Perdew, K. Burke and M. Ernzerhof, *Phys. Rev. Lett.*, 1996, **77**, 3865–3868.
45 S. Grimme, J. Antony, S. Ehrlich and H. Krieg, *J. Chem. Phys.*, 2010, **132**, 154104.
46 P. E. Blöchl, *Phys. Rev. B: Condens. Matter Mater. Phys.*, 1994, **50**, 17953–17979.
47 G. Kresse and D. Joubert, *Phys. Rev. B: Condens. Matter Mater. Phys.*, 1999, **59**, 1758–1775.
48 J. P. Perdew, M. Ernzerhof and K. Burke, *J. Chem. Phys.*, 1996, **105**, 9982–9985.
49 C. Adamo and V. Barone, *J. Chem. Phys.*, 1999, **110**, 6158–6170.
50 G. Di Liberto, L. A. Cipriano and G. Pacchioni, *ACS Catal.*, 2022, **12**, 5846–5856.
51 J. K. Nørskov, T. Bligaard, A. Logadottir, J. R. Kitchin, J. G. Chen, S. Pandelov and U. Stimming, *J. Electrochem. Soc.*, 2005, **152**, J23.
52 J. K. Nørskov, T. Bligaard, J. Rossmeisl and C. H. Christensen, *Nat. Chem.*, 2009, **1**, 37–46.
53 E. Di Simone, G. Vilé, G. Di Liberto and G. Pacchioni, *ACS Catal.*, 2025, **15**, 447–456.
54 B. Ravel and M. Newville, *J. Synchrotron Radiat.*, 2005, **12**, 537–541.
55 *Aspen Plus 11*, Aspen Technology Inc., Bedford, MA, USA, 2019.
56 *Aspen Plus 11 User Guide*, Aspen Technology Inc., Bedford, MA, USA, 2019.
57 Sigma-Aldrich, Merck KGaA, Darmstadt, Germany, https://www.sigmaaldrich.com/IT/it (accessed July 6, 2025).
58 ISO, *ISO* 14040*: Environmental management, life cycle assessment, principles and framework*, 2006; https://www.iso.org/standard/37456.html (accessed July 6, 2025).
59 L. Benini, S. Sala, S. Manfredi and M. Góralczyk, *Quantitative Methods for Life Cycle Assessment*, Publications Office of the European Union, Luxembourg, 2014, p. JRC92824.
60 K. Richardson, W. Steffen, W. Lucht, J. Bendtsen, S. E. Cornell, J. F. Donges, M. Drüke, I. Fetzer, G. Bala, W. von Bloh, G. Feulner, S. Fiedler, D. Gerten, T. Gleeson, M. Hofmann, W. N. Huiskamp, M. Kummu, C. Mohan, D. Nogués-Bravo, S. Petri, M. Porkka, S. Rahmstorf, S. Schaphoff, K. Thonicke, A. Tobian, V. Virkki, L. Wang-Erlandsson, L. Weber and J. Rockström, *Sci. Adv.*, 2023, **9**, eadh2458.
61 M. A. J. Huijbregts, Z. J. N. Steinmann, P. M. F. Elshout, G. Stam, F. Verones, M. Vieira, M. Zijp, A. Hollander and R. van Zelm, *Int. J. Life Cycle Assess.*, 2017, **22**, 138–147.
62 S. Andreasi Bassi, F. Biganzoli, N. Ferrara, A. Amadei, A. Valente, S. Sala and F. Ardente, *Updated characterisation and normalisation factors for the Environmental Footprint 3.1 method*, Publications Office of the European Union, Luxembourg, 2023, p. JRC130796.

